PAPER

Check for updates

The effect of the metal and selenium precursors on the properties of NbSe₂ and Nb₂Se₉ nanostructures and their application in dye-sensitized solar cells†

T. Kolokoto,[a] V. Mashindi,[a] R. Kadzutu-Sithole,[a] Lerato F. E. Machogo-Phao,[ab] Z. B. Ndala,[a] N. P. Shumbula,[a] S. S. Nkabinde,[a] G. N. Ngubeni,[a] S. S. Gqoba,[a] K. P. Mubiayi*[a] and N. Moloto [ID] *[a]

Herein, we report on the effect of the precursors on the structural, morphological, and optical properties of niobium selenide using the heat-up colloidal method. The metal precursor was varied from the conventional $NbCl_5$ to NbF_5 whilst Se, SeO_2, and selenourea were used as the selenium precursors. The $NbCl_5$ and NbF_5 resulted in the formation of $NbSe_2$ and Nb_2Se_9 respectively. While maintaining the two different metal precursors and varying the selenium precursor from Se, SeO_2 to selenourea, the properties of $NbSe_2$ and Nb_2Se_9 changed slightly, however the effect of changing the selenium precursor was less pronounced than changing the metal precursors. From the XRD and XPS, the $NbSe_2$ nanostructures were more susceptible to oxidation than Nb_2Se_9 as Nb_2O_5 was observed in the XRD and the percentage of M–O in the XPS was much higher in $NbSe_2$. $NbSe_2$ formed nanoflowers whilst Nb_2Se_9 formed rods with 3.29 eV and 2.43 eV band-gaps, respectively. Also, the band-gaps were red-shifted as the selenium precursors were varied. The $NbSe_2$ nanoflowers and Nb_2Se_9 nanorods were used as counter electrodes in dye-sensitized solar cells. Two methods were used to fabricate the counter electrodes *i.e.* spin coating and drop casting. The electrochemical properties of the spin coated counter electrodes were better than the drop casted ones; hence, they were employed in dye-sensitized solar cells. The spin coated $NbSe_2$ nanoflowers had the highest efficiency of 6.84%, attributed to the nanoflower morphology.

1. Introduction

2D layered materials such as $MoSe_2$, WSe_2, and graphene are fast becoming some of the most interesting materials. Their unique properties such as optical, electronic, and tribological properties have resulted in their use in various applications and technologies including photovoltaics, field-effect transistors, biosensors, and lubricants to name a few.[1–3] The research into these materials is forever expanding and less explored materials are being investigated. One such material is niobium selenide. Niobium selenide is a layered transition metal chalcogenide material that crystallizes in many stoichiometric forms such as $NbSe_2$, Nb_2Se, Nb_2Se_3, $NbSe_3$, Nb_3Se_4, and Nb_2Se_9. The syntheses of these materials have been largely confined to solid-state syntheses such as the direct reaction of Nb metal with Se in a sealed quartz tube at elevated temperatures and the

exfoliation of bulk $NbSe_2$ to form nanosheets.[4–6] A summary of the various synthetic routes that have been used to synthesize these materials is tabulated in Table 1. However, as much as these techniques have been successful in synthesizing $NbSe_2$ and Nb_2Se_9, they have limitations such as the need for high temperatures and pressure; as such, there is room for improvement. There have been a few reports on the colloidal synthesis (heat-up or hot-injection) of niobium selenide.

Sekar and co-workers reported on the synthesis of $NbSe_2$ nanoplates and nanowires using the heat-up colloidal method. Different morphologies were formed by quenching the hot reaction mixture at different temperatures.[14] Also recently, Guo *et al.* reported that upon changing the cooling rate, the morphology changed from spherical $NbSe_2$ to nanorod $NbSe_2$.[15] The colloidal synthesis involves the thermolyzation of precursors in a high boiling solvent to yield nanomaterials with controlled sizes and shapes. The formation of the nanomaterials is governed by the Lamer and Dinegar growth mechanism, where initially, nucleation occurs followed by the growth of the nuclei.[16] In the heat-up colloidal method, all reagents are mixed at room temperature and then heated up controllably to initiate the nucleation and growth of the nanoparticles. At room temperature, the reaction mixture is comprised mainly of

[a]*Molecular Sciences Institute, School of Chemistry, University of the Witwatersrand, Private Bag 3, Wits, 2050, South Africa. E-mail: Kalenga.Mubiayi@wits.ac.za; Nosipho.Moloto@wits.ac.za; Tel: +27 11 717 6720; +27 11 717 6774*

[b]*Analytical Services Division, Mintek, 200 Malibongwe Drive, Randburg, South Africa*
† Electronic supplementary information (ESI) available. See DOI: 10.1039/d0ra10894d

Table 1 Summary of the different methods used to synthesize niobium selenide materials, specifically Nb_2Se_9 and $NbSe_2$

Material	Synthetic method	Properties	Reference
$NbSe_2$	(a) mechanical exfoliation	(a) 1 μm to 30 μm with a thickness less than 2 μm	7
	(b) liquid exfoliation	(b) micro/nanoplatets range from 0.1 μm to 25 μm with a thickness less than 1 μm	8
	(c) RF magnetron sputtering	(c) 1.5 μm in thickness	9
	(d) chemical vapor transport	(d) 10 mm flakes	10
Nb_2Se_9	(a) flux method	(a) 117 nm to 547 nm nanowires	11
	(b) mechanical exfoliation	(b) 30 nm to 160 nm flakes	12
	(c) sintering in evacuated quartz tube	(c) single crystals	13

precursors. These convert to monomers upon heating and this initiates the nucleation process. Further heating results in the growth of these nuclei into mature particles. The growth of the nanoparticles is quenched by removing from the heat.

Careful consideration of the choice of precursors and ligands is therefore required in the heat-up method to ensure that nucleation is rapid to generate large quantities of nano-sized nuclei within a relatively short time and that the appropriate decoupling of the nucleation and growth stages occurs to reduce particle polydispersity.[17] In addition, different precursors can result in different properties of the nanostructures. Herein, for the first time, we report on a systematic study on the effect of the precursors on the structural, morphological, and optical properties of niobium selenide using the heat-up colloidal method. Both the metal precursors and the selenium precursors were investigated. The metal precursor was varied from the conventional $NbCl_5$ to NbF_5 whilst Se, SeO_2, and selenourea were used as the selenium precursors. Furthermore, we elucidate the mechanism of formation for both $NbSe_2$ and Nb_2Se_9 nanostructures.

Inorganic nanomaterials have been used in solar cells for different roles ranging from absorber-layers to buffer layers, to sensitizing material in quantum dot sensitized solar cell and counter electrodes (CEs) in dye-sensitized solar cells (DSSCs).[18] This is due to their unique properties such as material diversity, abundance, low cost, high catalytic activity, and ease of modification.[18] For dye sensitized solar cell CEs, Pt has been the benchmark due to its good conductivity and superior catalytic activity towards the reduction of triiodide (I_3^-) to iodide (I^-). However, Pt is an expensive noble metal and is susceptible to corrosion by the electrolyte over time. Therefore current studies are focused on finding alternatives to Pt. 2D materials have been

of interest due to their high optical transparency and high catalytic activity.[19] Liang *et al.* used ultrathin MoS_2 nanofilms as CEs in DSSCs where their cyclic voltammetry revealed that they possessed excellent catalytic activity towards the reduction of I_3^-.[20] Ibrahem *et al.* and Guo *et al.* reported on the use of $NbSe_2$ nanosheets as CEs in DSSCs with solar conversion efficiencies of 7.73% and 7.34%, respectively.[21,22] Herein, $NbSe_2$ nanoflowers and Nb_2Se_9 nanorods were investigated as potential CE for DSSCs.

2. Experimental section

Chemicals

Niobium(v) chloride 99%, niobium(v) fluoride 98%, elemental selenium powder, 99.9% selenium dioxide, 98% selenourea (SU), 70% oleylamine (OLA), 95% hexane, 96% ethanol, 98% toluene, 99% isopropanol, 96% methanol, 99.9% acetonitrile, 99.9% lithium iodide, 95% lithium perchlorate, 99.9% sodium iodide, 99.8% iodine, 98% 4-*tert*-butylpyridine, fluorine doped tin oxide (FTO, 7 Ω sq^{-1}), white titania paste (TiO_2, 20.0 wt%), and N-719 dye (95%) were all purchased from Sigma-Aldrich.

Syntheses of niobium selenide nanostructures

Varying the metal precursor. Oleylamine was placed in a three-necked round bottom flask and degassed for 15 min. This was followed by a 1 : 4 stoichiometric addition of $NbCl_5$ or NbF_5 and Se. The mixture with a concentration of 0.125 M was further degassed for 10 min under vigorous stirring before being heated to 320 °C. After 120 min the mixture was cooled naturally to room temperature and the black precipitate was washed with large amounts of ethanol and hexane mixture, air-dried, and ready for characterization.

Table 2 Summary of the reaction conditions for the synthesis of $NbSe_2$ and Nb_2Se_9 nanostructures

Sample	Metal precursor	Selenium precursor	Capping agent	Concentration	Temperature	Time
1	$NbCl_5$	Se	OLA	0.125 M	320 °C	120 min
2	NbF_5	Se	OLA	0.125 M	320 °C	120 min
3	$NbCl_5$	SeO_2	OLA	0.125 M	320 °C	120 min
4	$NbCl_5$	SU	OLA	0.125 M	320 °C	120 min
5	NbF_5	SeO_2	OLA	0.125 M	320 °C	120 min
6	NbF_5	SU	OLA	0.125 M	320 °C	120 min

Varying the selenium precursor. The same procedure as above was followed; however, the selenium precursors were varied to SeO_2 and SU. The summary of all the reaction parameters is tabulated in Table 2.

Characterization of the nanostructures

The structure and phase of the powdered materials were determined with the Bruker MeasSrv (D2-205530)/D2-205530 diffractometer using secondary graphite monochromated CuKα radiation (λ 1.54184 Å) at 30 kV/30 mA. Measurements were taken using a glancing angle of incidence detector at an angle of $2°$, for 2θ values over $10–90°$ in steps of $0.026°$ with a step time of 37 s and at a temperature of 25 °C. X-ray photoelectron spectroscopy measurements were performed with a Thermo ESCAlab 250Xi using monochromatic Al Kα (1486.7 eV) X-rays at a power of 300 W with a spot size 900 μm. The morphologies were studied using an FEI Nova Nanolab 600 FIB/SEM scanning electron microscope (SEM) equipped with an EDX detector.

The powder samples were mounted on aluminium stubs with carbon tape. An FEI Spirit 120 kV transmission electron microscope (TEM) equipped with an EDX detector operated at an acceleration voltage of 200 kV with a beam spot size of 20–100 nm in TEM mode was also used. The particles were dispersed in hexane and drop-casted onto a lacey carbon copper grid. The solvent was then evaporated at room temperature. A Specord 50 Analytik Jena UV-vis spectrophotometer was used to carry out the absorption measurements. The particles were dissolved in hexane and placed in a quartz cuvette (1 cm path length).

Fabrication of the counter electrodes

The nanoparticles were dissolved in toluene and the mixture was sonicated for 30 min to form an ink. The FTO-glass substrate was cleaned with soap-water and sonicated for 15 min. The slides were rinsed with distilled water and sonicated further for another 15 min and lastly with isopropanol and sonicated for 15 min. The slides were left to dry before the ink was deposited onto them. Two methods for depositing the ink were used:

(i) Drop-casting: the ink was drop-casted onto a clean FTO-glass slide and left to dry at room temperature. The thin film was baked for 60 min at 120 °C in an oven.

(ii) Spin-coating: the ink was deposited onto the substrate and a spin-coater CHEMAT technology KW-4A was used to spread the ink uniformly. The thin film was baked for 60 min at 120 °C in an oven.

The Pt-CE was formed by sputter-coating three coats of Pt onto a clean FTO-glass slide using a Cressington 108auto/SE sputter coater with a thickness controller MTM-20. A 50 nm Pt film was formed.

Photoanode fabrication

Titania (TiO_2) paste was printed onto pre-cleaned FTO substrates using the doctor blade method. The screen-printed substrates were then annealed at 350 °C for 30 min to remove any residual organic compounds and enable better contact between TiO_2 and the N-719 dye. The N-719 dye was then dissolved in methanol (3.0×10^{-4} M) and used to sensitize the TiO_2. A drop of the dye mixture was placed onto the annealed TiO_2 and left to dry overnight, in the dark at ambient conditions.

Device assembly

The photoanode electrode was placed with the active layer facing up and the counter electrode facing down. The two electrodes were offset from each other and the Whatman filter paper was placed in between to define the active area and act as a sponge for the supporting redox electrolyte solution. The supporting redox electrolyte solution, which provides a negative electrochemical potential for the reduction process, was composed of 0.05 M iodine, 0.1 M lithium iodide, 0.1 M potassium iodide, 0.1 M sodium iodide and 0.5 M 4-tert-butyl-pyridine. The assembled device was held together lengthwise by the fold back clips on both sides to create uniform distribution.

Characterization of the electrodes

Cyclic voltammetry (CV), electrochemical impedance (EIS), and Tafel polarization measurements were done using Biologic: VMP 300. A three-electrode system was used to conduct the CV measurements using the triiodide (I^-/I_3^-) redox electrolyte composed from 0.1 M $LiClO_4$, 0.01 M LiI, and 0.001 M I_2 dissolved in anhydrous acetonitrile using Pt as the counter electrode, Ag/AgCl as the reference electrode and the synthesized $NbSe_2$ and Nb_2Se_9 as the working electrodes after being drop-casted on a glassy carbon electrode (GC, active area $\sim$ 0.07 cm², platinum (Pt, active area = 0.05 cm²), and FTO (active area $\sim$ 1.56 cm²), respectively. EIS measurements were obtained using a symmetrical cell with two identical electrodes in the redox electrolyte used for DSSCs in the dark. The electrodes were analysed between 100 kHz and 100 MHz at varying open circuit potentials for each sample. The Tafel polarization analysis was conducted at a potential window of −1.0 to 1.0 V with a scan rate of 100 mV s^{-1}. The photocurrent–voltage ($J–V$) characteristic curves of the DSCCs were measured in ambient conditions using the HP 4141B source measure unit (SMU) under controlled illumination of 100 mW cm^{-2} (AM 1.5G).

3. Results and discussion

Varying the niobium precursor

Metal precursors have been shown to influence the properties of nanostructures due to their reactivity. Metal chlorides, acetate, and nitrates have been commonly used as precursors for synthesis of both metal chalcogenides and oxides. Herein, the effect of using $NbCl_5$ and NbF_5 on the resultant nanostructures was investigated. Shown in Fig. 1 are the X-ray diffraction patterns of particles synthesized by varying the niobium precursor. The use of $NbCl_5$ resulted in the formation of 2H–$NbSe_2$ (PDF 01-070-5612) and also oxide impurities in the form of T–Nb_2O_5 denoted by # (PDF 30-0873). Changing the precursor

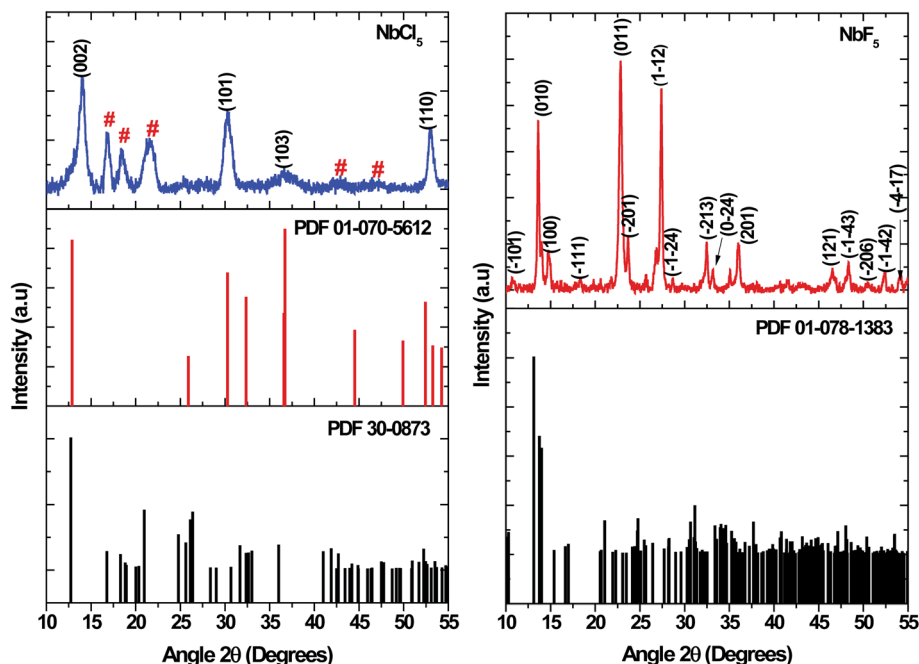**Fig. 1** XRD patterns of particles synthesized from $NbCl_5$ and NbF_5 precursors.

to NbF_5 resulted in the formation of Nb_2Se_9 (PDF 01-078-1383), with no impurities detected.

The two stoichiometries ($NbSe_2$ and Nb_2Se_9), differ in structure as shown in Fig. 2. $NbSe_2$ has a crystal structure containing polymeric layers with the Nb-layer sandwiched between two Se-layers (*i.e.* Se–Nb–Se). The Nb and Se atoms are covalently bonded whilst each polymeric layer is held together by weak van der Waals interactions. The layers are closely
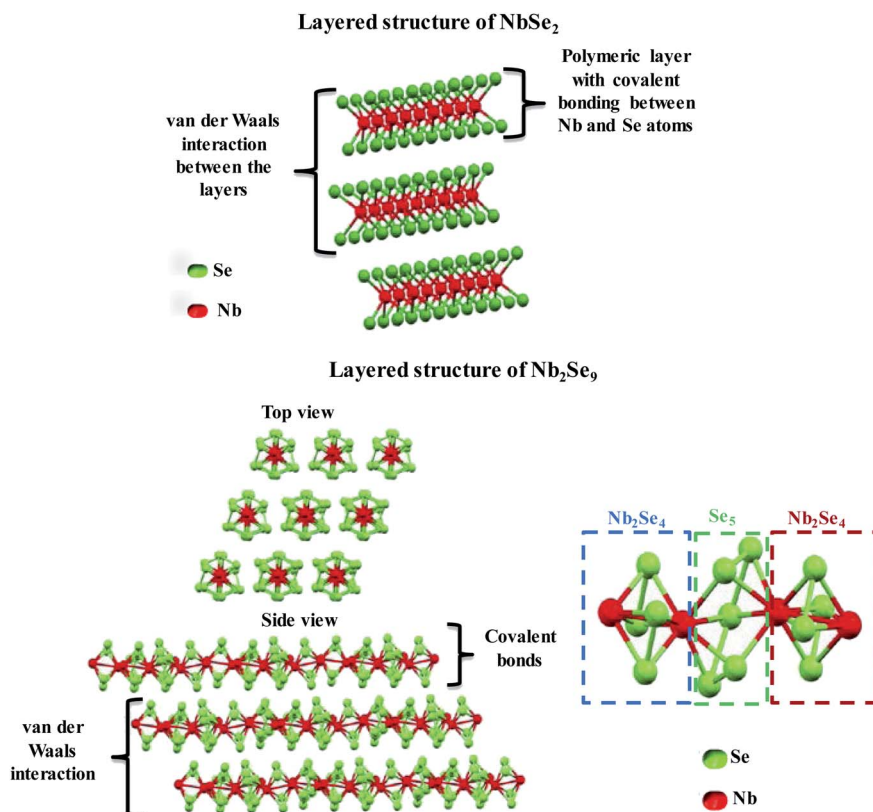
Fig. 2 Chemical structure of $NbSe_2$ and Nb_2Se_9 layered materials.
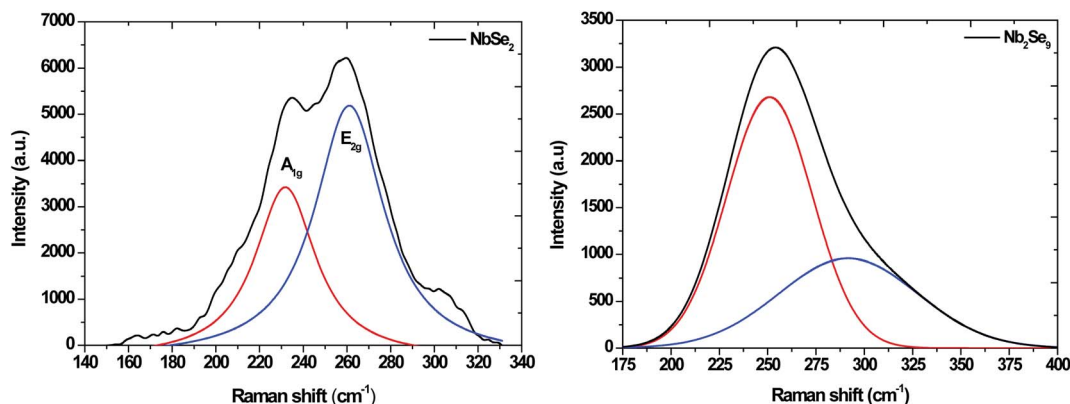
Fig. 3 Raman spectra of $NbSe_2$ and Nb_2Se_9 materials synthesized from when varying the niobium precursors.

packed and the arrangement of up to 6 layered structures has been reported.[23] The weak van der Waals forces are responsible for the easy sliding of the layers relative to one another, thus providing a favourable matrix for intercalation reactions and exfoliation.[24] The coordination around the Nb atom can either be a distorted octahedral or trigonal prismatic.[23] On the other hand, Nb_2Se_9 is a new 1D material made up of periodically stacked single-chain atomic crystals, which form the inorganic bulk of the crystals due to strong covalent bonds within the chain and weak van der Waals interaction between the chains, as shown in Fig. 2.[25] It is similar to the structure of $NbSe_2$ but it has chains and not polymeric sheets. Each Nb_2Se_9 chain is

made up of Nb_2Se_4–Se_5–Nb_2Se_4–Se_5 sequence along the c-axis.[24,25] Nb_2Se_4 forms a cage, each Nb atom is surrounded by one Se_5 and two Se_2 units thus coordinated to eight Se atoms.[25] Therefore, Nb can be considered to have bicapped-trigonal prismatic coordination around it. The Nb atoms form non-linear chains because of the alternating long and short bonds with distances of 3.76 Å and 2.89 Å, respectively.[25]

The Raman spectra for $NbSe_2$ and Nb_2Se_9 are shown in Fig. 3. The $NbSe_2$ spectrum has two characteristic peaks, the out of plane A_{1g} peak and the in plane E_{2g} peak at 225 and $\sim$245 cm^{-1}, respectively.[26] On the other hand, the vibrational modes of Nb_2Se_9 were at 239.62 cm^{-1} due to two Nb atoms vibrating along the (101) plane and the two Se pairs with a stretching motion.[27] The second vibrational motion at 284.18 cm^{-1} was due to two pairs of stretching Nb atoms crossed and all the Se atoms vibrating in the outward direction at the same time.[28]

To further elucidate the structures, XPS was undertaken. Shown in Fig. 4 are the XPS survey spectra of the as-synthesized particles. Both spectra showed the presence of Nb, Se, C and O. The C is due to the capping agent and the O is because of the oxidation of the capping agent as well as the Nb_2O_5 in the $NbCl_5$ derived particles as observed in XRD.

To fully understand the chemical species present, high-resolution spectra were recorded. The C1s and O1s for both $NbSe_2$ and Nb_2Se_9 particles showed a presence of C–C, C–O, and C=O emanating from the capping agent (Fig. 1S†). The C–O and C=O bonds are indicative of oxidation of the capping agent.[29] As such the capping does provide a protective layer and hence minimizes the oxidation of the core inorganic particle. Nevertheless, some oxidation of the inorganic core was observed as evidenced by the detection of an M–O species in both $NbSe_2$ and Nb_2Se_9 O1s core level spectra. The extent of the oxidation is however different. The $NbSe_2$ was more oxidized than Nb_2Se_9 as shown in Table 3 and also observed as T–Nb_2O_5 in the XRD pattern.

Fig. 5 shows the Nb3d and Se3d core-level spectra of $NbCl_5$ and NbF_5 derived $NbSe_2$ and Nb_2Se_9 nanostructures respectively. The $NbSe_2$ Nb3d core level spectrum showed three components, composed of the $Nb^{4+}3d_{5/2}$ (203.0 eV), the $Nb^{5+}3d_{5/2}$ (206.9 eV) and the $Nb^{5+}3d_{3/2}$ (209.3 eV). The $Nb^{4+}3d_{5/2}$
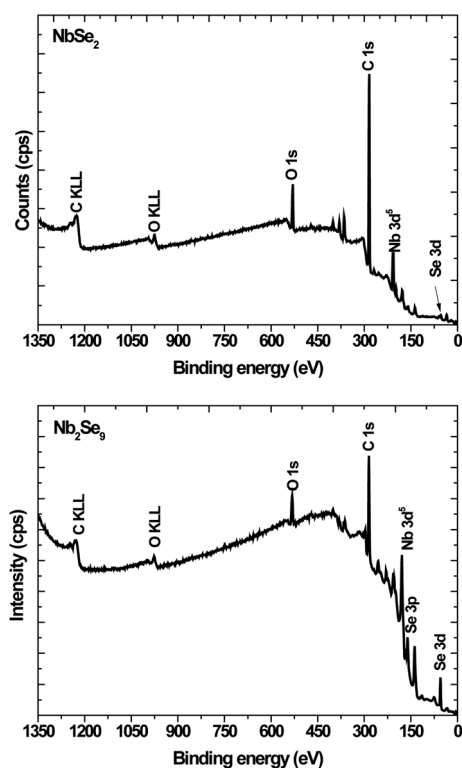

Fig. 4 XPS survey spectra of $NbSe_2$ and Nb_2Se_9 when varying the niobium precursors.

Table 3 Summary of the atomic composition and stoichiometric assignments obtained from the fitting of the XPS spectra reported in ESI Fig. 1S and 5

Precursor	Element	Atomic%	Peak binding energy (eV)	Assignments	Assignment%
$NbCl_5$	C	85.3	284.8	C–C	78.6
			286.3	C–O	4.7
			288.8	O–C=O	1.9
	O	10.2	530.2	M–O	5.4
			531.7	C=O	4.1
			533.3	C–O	2.4
	Nb	2.9	203.0	$Nb^{4+}3d_{5/2}$	0.1
			206.9	$Nb^{5+}3d_{5/2}$	1.5
			209.3	$Nb^{5+}3d_{3/2}$	0.4
	Se	1.5	53.4	$Se3d_{5/2}$	0.7
			55.5	$Se3d_{3/2}$	0.6
NbF_5	C	77.9	284.9	C–C	59.5
			286.2	C–O	6.0
			288.7	O–C=O	4.1
	O	13.3	530.1	M–O	2.8
			531.8	C=O	5.5
			533.6	C–O	4.4
	Nb	2.5	203.6	$Nb^{4+}3d_{5/2}$	1.6
			206.3	$Nb^{4+}3d_{5/2}$	1.6
			207.3	$Nb^{5+}3d_{3/2}$	1.3
			210.1	$Nb^{5+}3d_{5/2}$	1.6
	Se	6.3	54.2	$Se3d_{5/2}$	8.3
			55.4	$Se3d_{3/2}$	3.7

and the $Nb^{4+}3d_{3/2}$ peaks corresponded to $NbSe_2$ while the $Nb^{5+}3d_{5/2}$ corresponded to Nb_2O_5. These results were consistent with work reported by Boscher et al.[30] The $NbSe_2$ Se3d core level spectrum showed two peaks all attributed to the $NbSe_2$.

For Nb_2Se_9, the Nb3d core level spectrum showed four peaks assigned to $Nb^{4+}3d_{5/2}$ (203.6 eV), $Nb^{4+}3d_{5/2}$ (206.3 eV), $Nb^{5+}3d_{5/2}$ (207.3 eV), and $Nb^{5+}3d_{5/2}$ (210.0 eV) corresponding to Nb_2Se_9 and Nb_2O_5 similar to the $NbSe_2$ spectrum. The XRD pattern of NbF_5 derived particles showed no evidence of Nb_2O_5. This suggests that the extent of metal oxidation is not as pronounced in Nb_2Se_9 since XRD is a bulk technique. The % composition of the present chemical species is summarized in Table 3. The % atomic composition of O was more in NbF_5 derived particles compared to $NbCl_5$ derived particles (13.3% and 10.2% respectively), however from the assignment%, NbF_5 derived particles had the least amount attributed to M–O (2.8%) suggesting that most of the oxidation occurred in the organic capping layer.

The nature of the capping of the nanostructures can be further investigated using FT-IR and spectroscopy. The FT-IR spectra of the as-synthesized OLA-capped $NbSe_2$ and Nb_2Se_9 nanostructures are illustrated in Fig. 6. Three main functional groups were identified in pure OLA. These functional groups were C–N, CH_2/CH_3 and N–H. The C–N and N–H peaks located at 1071 cm^{-1} and 1593 cm^{-1} respectively, decreased in intensity in the $NbSe_2$ spectrum compared to the pure OLA. On the other
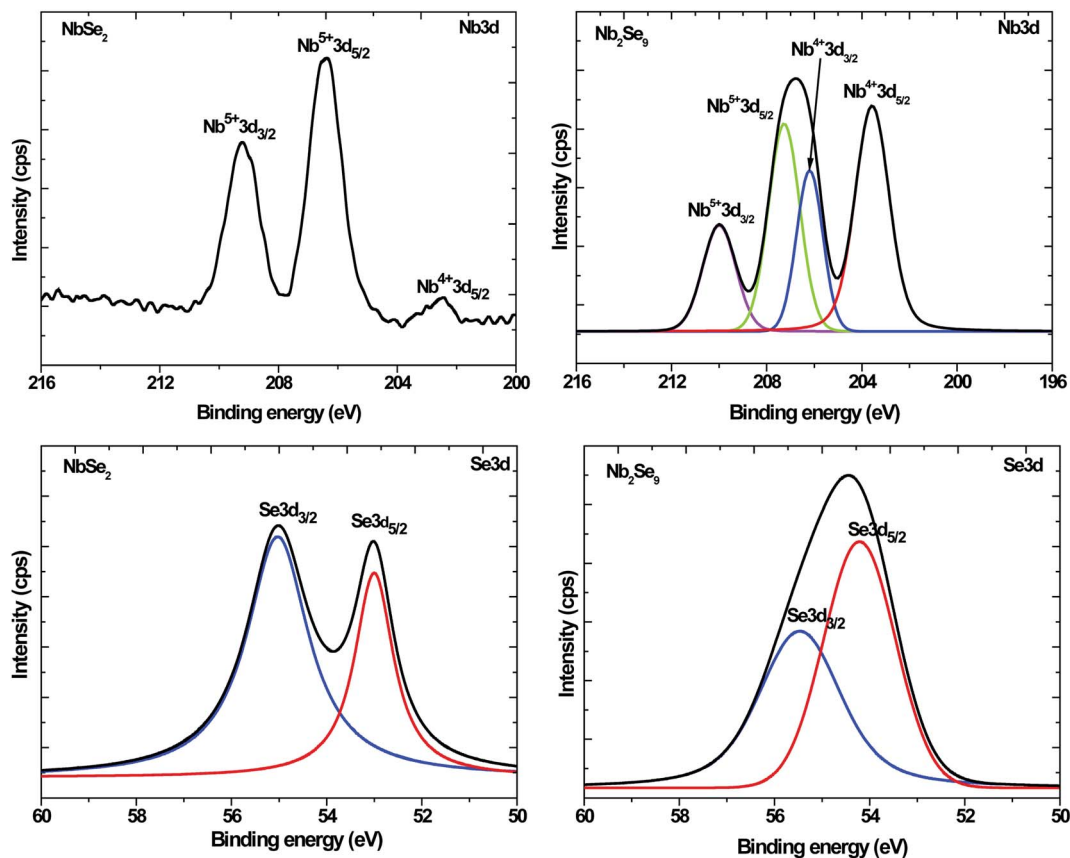
Fig. 5 Nb3d and Se3d XPS core-level spectra for $NbSe_2$ and Nb_2Se_9 when varying the niobium precursors.
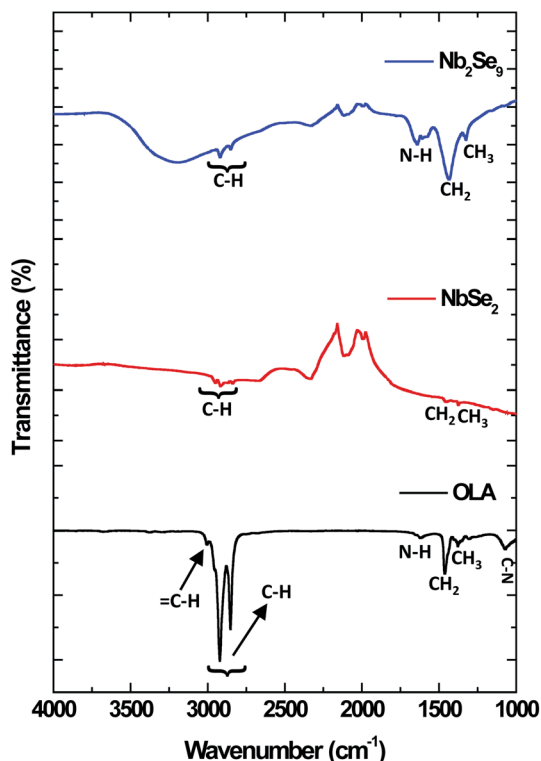
Fig. 6 FT-IR spectra of oleylamine (OLA), $NbSe_2$ and Nb_2Se_9 when varying the niobium precursors.

hand, in the FT-IR spectrum of Nb_2Se_9, the C–N peak disappeared and the N–H peak was shifted as well as broadened compared to the pure OLA. This confirms that there is a change in the terminal functional group (–NH_2) in OLA. As such, this further confirms that OLA has capped the surface of these nanostructures.[31]

To study the morphological properties of the resultant materials, SEM and TEM studies were undertaken. Shown in Fig. 7 are the SEM and TEM images of the particles synthesized from the two metal precursors. The $NbSe_2$ particles showed sheet-like morphology. This is consistent with 2D layered materials. From SEM, the sheets are arranged in a flower-like pattern. Colloidal synthesized nanosheets tend to have high surface energies hence they fold over each other forming architectures such as the nanoflowers to minimize the surface energy.[32] Although the focus of many studies has been on flat nanosheets, assembly into 3D nanoflowers has advantages such as high specific surface area, broad internal space, mechanical stability, and easy accessibility to catalytically active sites.[33] The presence of many edge sites is advantageous for electrocatalytic applications as edge sites are more catalytically active than the basal planes of the material.[34] On the other hand, NbF_5 derived particles showed rod-like morphology. The rod-like structures are consistent with the crystal structure of Nb_2Se_9 shown in Fig. 2. This is also in line with the work reported by Lee *et al.*[4]

To study the optical properties of the resultant materials, UV-vis absorption spectroscopy was undertaken and the results are
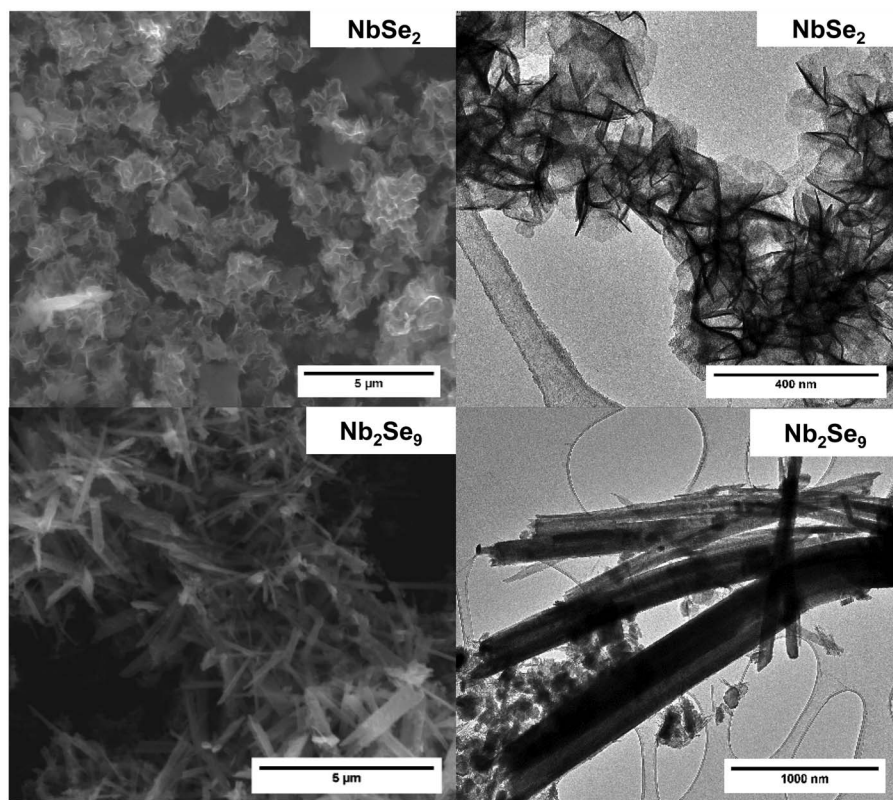

Fig. 7 SEM and TEM micrographs of $NbSe_2$ and Nb_2Se_9 when varying the niobium precursors.
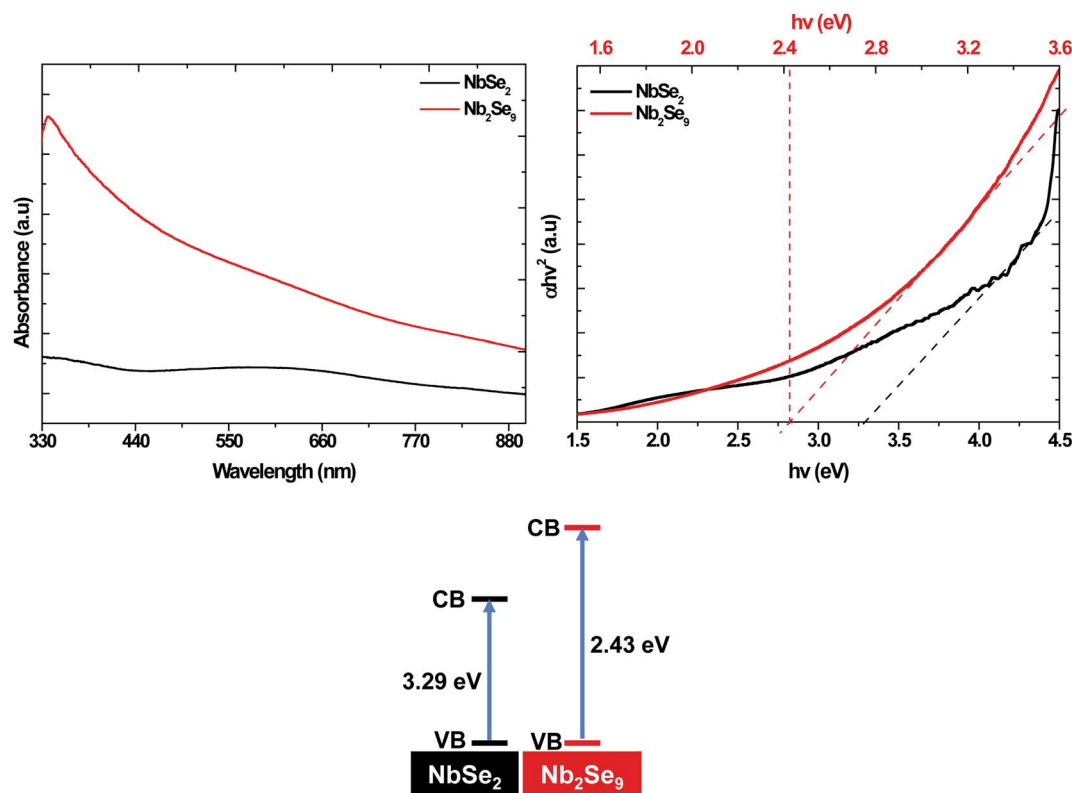
Fig. 8 UV-vis absorption spectra and Tauc plot of $NbSe_2$ and Nb_2Se_9 when varying the niobium precursors.

shown in Fig. 8. The band-gap of $NbSe_2$ (3.29 eV) was firmly on the UV region while the band-gap of Nb_2Se_9 was in the visible region (2.43 eV). This suggests that by altering the precursor, one can alter the optical properties.

Based on the obtained results, the mechanism of formation of $NbSe_2$ and Nb_2Se_9 was deduced. In the colloidal heat-up method, the decomposition of the precursors (Fig. 9) drives the formation of the nuclei. Based on the HSAB theory, Nb^{5+} is a hard Lewis acid, and F^- is a harder Lewis base compared to Cl^-, as such, Nb^{5+} forms a more stable complex with F^- than Cl^-.[35] As a result, the decomposition chemistry of the two compounds will be different. Nb^{5+} has tightly held outer electrons and vacant orbitals available that are not too high in energy. These orbitals can accept electrons from the ligand such as F to form π bonds.[35] Also, pentahalides have diversity in their structure. For example, $NbCl_5$ has a dimer structure (i.e. two Cl bridges)[36] whereas NbF_5 has a tetramer structure (i.e. four F

bridges) within a single unit cell (Fig. 7).[37] In a typical dimer, there are $(NbCl_5)_2$ units, the bridge-bonds are longer and weak which causes the axial bonds to bend inward.[38] A tetramer structure of NbF_5 contains $(NbF_5)_4$ units, each unit are connected by an F-bridge forming a square.[38] Hence, the nucleation and growth process of nanoparticles will be affected. The formation of $NbSe_2$ and Nb_2Se_9 from $NbCl_5$ and NbF_5 respectively occur based on the following reactions:

$$2NbCl_5 + 4Se \rightarrow 2NbSe_2 + 5Cl_2 \qquad (1)$$

$$2NbF_5 + 9Se \rightarrow Nb_2Se_9 + 5F_2 \qquad (2)$$
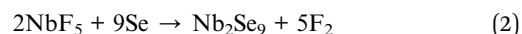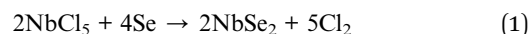
Using the TEM images of $NbSe_2$ and Nb_2Se_9 at different time intervals as shown in Fig. 10, the mechanism for the formation of the different morphologies is postulated. $NbSe_2$ nanoflowers begin with the formation of layered flocculates after 5 min which is essentially the starting material. Savjani et al. reported that MoS_2 initially forms flocculates, which are known to have lateral dimensions ranging from hundreds to thousands of nanometers.[39] Guo et al. reported that the formation of nanosheets is due to low supersaturation which allows growth to occur in two directions.[15] These lateral flocculates, slide over one another due to the weak van der Waals forces and begin to curl as shown in the 30 min sample. Finally, after 120 min nanoflowers are formed by completely curled nanosheets. Nb_2Se_9 nanostructures form quicker than $NbSe_2$ nanostructures as rods were already observed at 5 min. The formation of the rods is also postulated to form from layered flocculates and
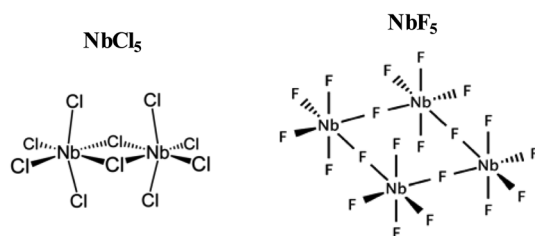

Fig. 9 Molecular structure of $NbCl_5$ and NbF_5.
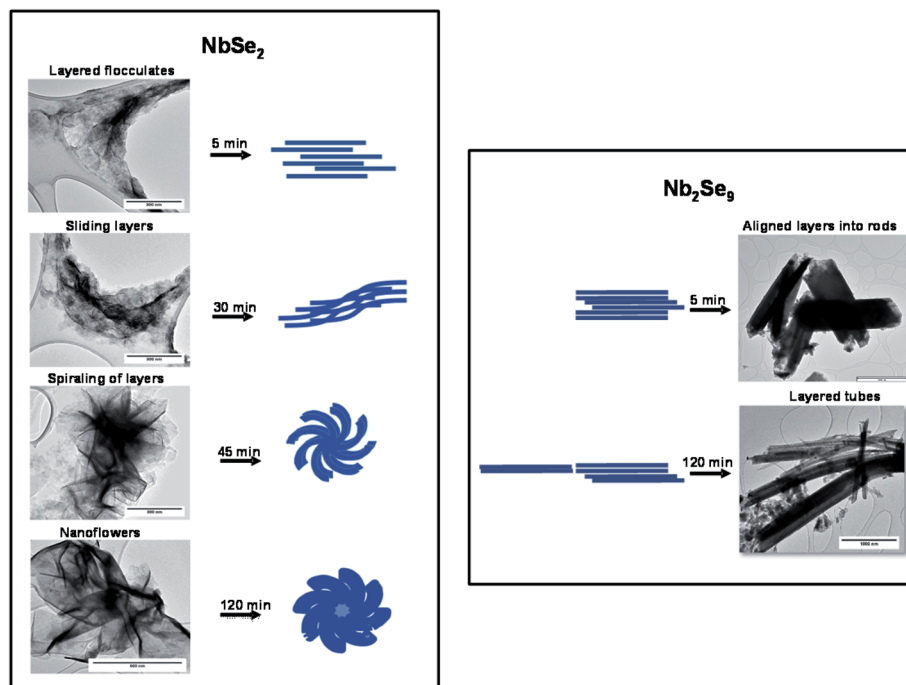
Fig. 10 Formation mechanism of NbSe₂ and Nb₂Se₉ when varying the niobium precursors.

these flocculates also slide over each other similar to NbSe₂, however, the sliding is not as pronounced. This is shown by the unevenness of the edges of the rods in the 5 min TEM image. After 120 min, the flocculates slide next to each forming chains that result in elongated rods. This is synonymous with the chain-like crystal structure expected for Nb₂Se₉. The small dot-

like particles on the image are thought to be Nb₂O₅ nanoparticles.

Varying the selenium precursor

Seeing that changing the metal precursor resulted in the formation of different niobium selenide crystal phases hence properties, the selenium precursors were also varied. Three
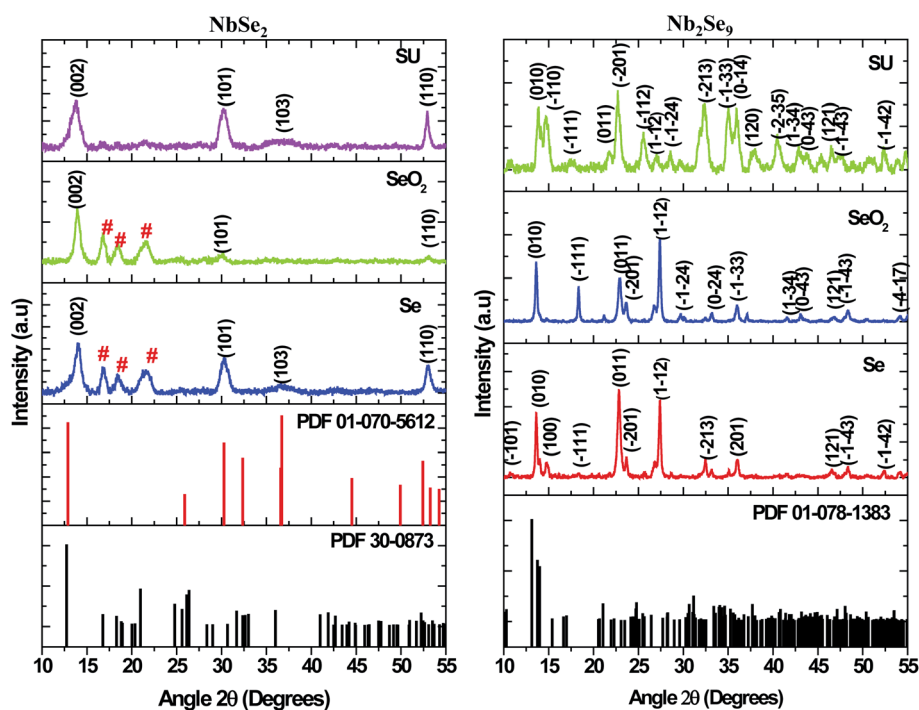

Fig. 11 XRD patterns of NbSe₂ and Nb₂Se₉ when varying the selenium precursors.

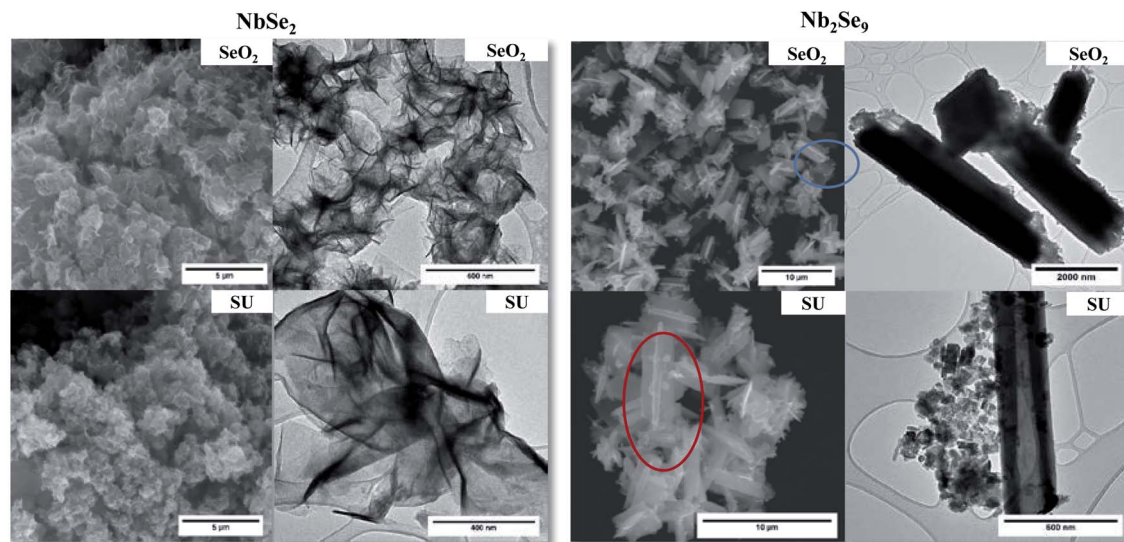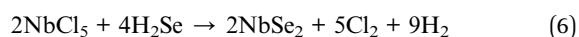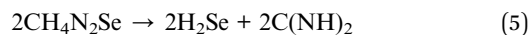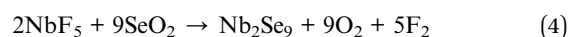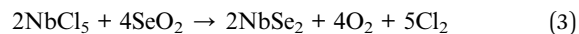**Fig. 12** SEM and TEM images of NbSe$_2$ and Nb$_2$Se$_9$ when varying the selenium precursors.

precursors were used, namely elemental selenium (Se), selenium dioxide (SeO$_2$), and selenourea (SU). Selenium is a non-metal that has similar properties to sulfur and tellurium. SeO$_2$ is a one-dimensional polymer that consists of alternating selenium and oxygen atoms. Each Se atom is pyramidal and bears a terminal oxide group. The stereochemistry at Se alternates along the polymer chain hence resulting in a syndiotactic polymer.[40] Selenourea is an organoselenium compound. This compound features an unhindered carbon–selenium double bond.

Shown in Fig. 11 are the X-ray diffractograms of NbSe$_2$ nanostructures emanating from NbCl$_5$ and different selenium precursors. The particles synthesized using Se as previously shown in Fig. 1 and SeO$_2$ were indexed to a hexagonal 2H–NbSe$_2$ phase (PDF 01-070-5612) indicated by the black *hkl* indices. Also, there were three high-intensity peaks (#) between 2θ values 15–25° indexed to an orthorhombic phase of T–Nb$_2$O$_5$ (PDF 30-0873). On the other hand, the particles synthesized from SU precursor were pure and consistent with a rhombohedral phase 3R–NbSe$_2$ (PDF 01-070-1620). The peak positions of the 2H–NbSe$_2$ and 3R–NbSe$_2$ are similar; however, there is a small shift towards lower angles for the rhombohedral phase as shown in Fig. 11. Also, the two phases have different lattice parameters, with a = 3.45 and c = 12.55 for the 2H-phase while a = 3.45 and c = 18.88 for the 3R-phase. The results from Nb$_2$Se$_9$ nanostructures emanating from NbF$_5$ and different selenium precursors are also shown in Fig. 11. The particles from the various selenium precursors were all indexed to a Nb$_2$Se$_9$ triclinic phase (PDF 01-078-1383). However, the intensities of the peaks were different as such the crystallinity. The peaks from Se and SeO$_2$ derived samples were more intense than the SU sample hence suggesting good crystallinity. The peak widths were much narrower for Se and SeO$_2$ than SU nanoparticles; therefore, indicative of different sizes. From the XRD results, it is quite clear that the metal precursors are responsible for the stoichiometry of niobium selenide, NbCl$_5$ result in NbSe$_2$ whilst NbF$_5$ results in Nb$_2$Se$_9$. In terms of the selenium precursors, Se

and SeO$_2$ due to their one-step reaction, they result in similar properties whilst SU involves a two-step synthetic route (first the decomposition of SU as in eqn (5) and the reaction with the metal precursors eqn (6) and (7)), as such, subtle differences in properties are observed. The reactions towards the formation of NbSe$_2$ and Nb$_2$Se$_9$ using the different selenium precursors are shown in eqn (1)–(7).

$$2NbCl_5 + 4SeO_2 \rightarrow 2NbSe_2 + 4O_2 + 5Cl_2 \tag{3}$$

$$2NbF_5 + 9SeO_2 \rightarrow Nb_2Se_9 + 9O_2 + 5F_2 \tag{4}$$

$$2CH_4N_2Se \rightarrow 2H_2Se + 2C(NH)_2 \tag{5}$$

$$2NbCl_5 + 4H_2Se \rightarrow 2NbSe_2 + 5Cl_2 + 9H_2 \tag{6}$$

$$2NbF_5 + 9H_2Se \rightarrow 2Nb_2Se_9 + 5F_2 + 9H_2 \tag{7}$$

The SEM and TEM images using the SeO$_2$ and SU as selenium precursors are shown in Fig. 12. For NbSe$_2$, varying the selenium precursor did not change the morphology; the particles remained flower-like nanosheets however the SU samples had larger nanoflowers. For Nb$_2$Se$_9$, there was a slight change of morphology from the Se precursor in Fig. 7 to the SeO$_2$ and SU precursors where perpendicular connected flat rods were formed as shown in the SEM images in Fig. 12. From the TEM,

Table 4 Summary of the band-gaps of NbSe$_2$ and Nb$_2$Se$_9$ when varying the selenium precursors

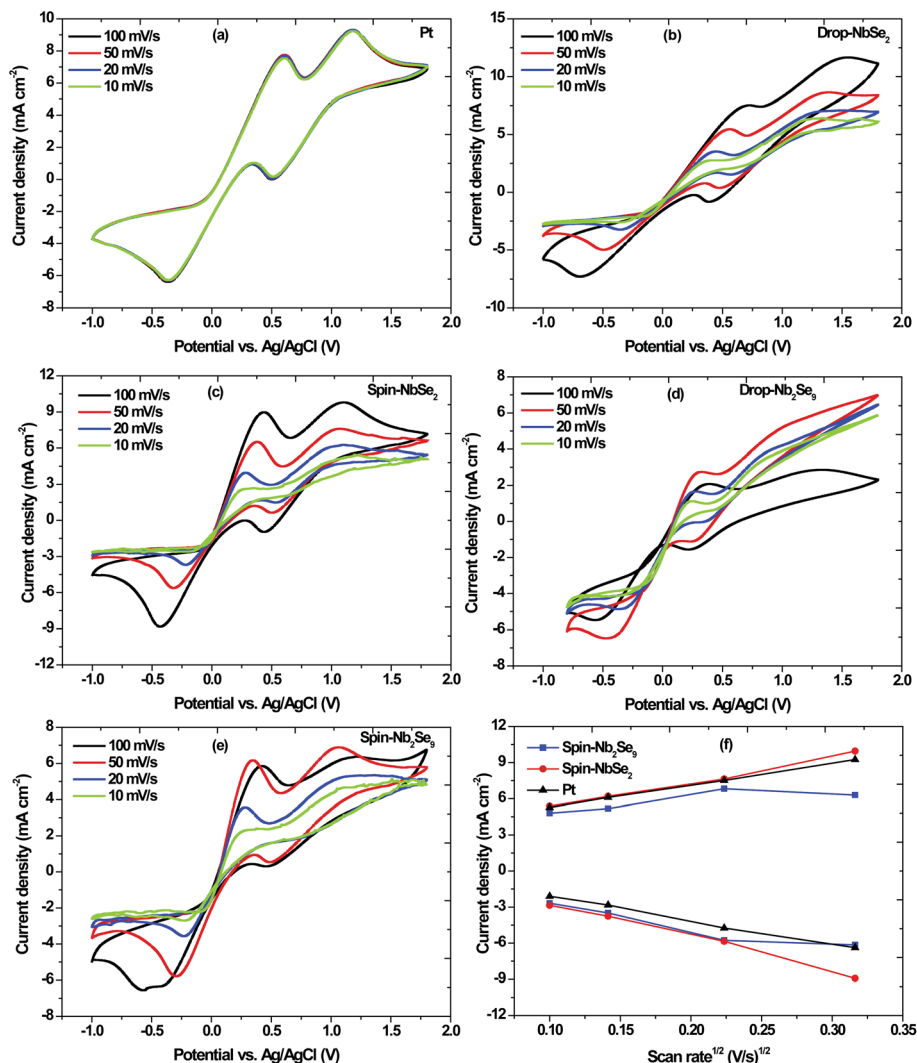| Selenium precursor	NbSe$_2$ E_g	Nb$_2$Se$_9$ E_g
Se	3.29 eV	2.43 eV
SeO$_2$	2.91 eV	2.44 eV
SU	2.55 eV	2.12 eV

Fig. 13 Cyclic voltammograms at different scan rates of (a) sputtered Pt, (b) drop casted NbSe$_2$, (c) spin coated NbSe$_2$, (d) drop casted Nb$_2$Se$_9$ and (e) spin coated Nb$_2$Se$_9$; and (f) linear fitting of the capacitive current densities of Pt compared with the NbSe$_2$ and Nb$_2$Se$_9$ CEs.

these were however very similar to the Se rods. HRTEM was also performed on the pure NbSe$_2$ and Nb$_2$Se$_9$ (shown in Fig. 2S†) which formed using SU. The average interlayer spacing for NbSe$_2$ layers is 0.61 nm, which is in agreement with the theoretical d-spacing for (002) planes.[41,42] The same spacing was obtained for Nb$_2$Se$_9$ nanorods.

The UV-vis absorption spectra of NbSe$_2$ and Nb$_2$Se$_9$ when varying the selenium precursors are shown in Fig. 3S† and the band-gap values are summarized in Table 4. For NbSe$_2$ nanoflowers, the band-gap decreases from Se to SeO$_2$ to SU. This is consistent with the observed increase in the size of the nanoflowers. An increase in size of the nanostructures results in the red-shift of the band-gap due to Ostwald ripening. The band-gap for Nb$_2$Se$_9$ remained relatively unchanged as the selenium precursor changed from Se to SeO$_2$. This is expected as there were little changes observed in the structural and morphological properties between the two precursors. The band-gap for SU was however red-shifted. It must be said that

from the absorption spectra in Fig. 3S,† the graphs were tailing suggesting polydispersity.

Application of NbSe$_2$ and Nb$_2$Se$_9$ as counter electrodes in DSSCs

NbSe$_2$ and Nb$_2$Se$_9$ nanostructures synthesized using SU as the selenium precursor were used as the counter electrodes. The electrocatalytic activity of the CEs was determined by cyclic voltammetry (CV), where the scan rate was varied to investigate the effect of the scan rate on the current density of each CE. Based on eqn (8), there exist a relationship between the current density and square root of the scan rate. As such, an increase in scan rate causes the diffusion layer thickness to decrease and the electrochemical polarization to increase which results in high overpotential and poor reversibility.[43]

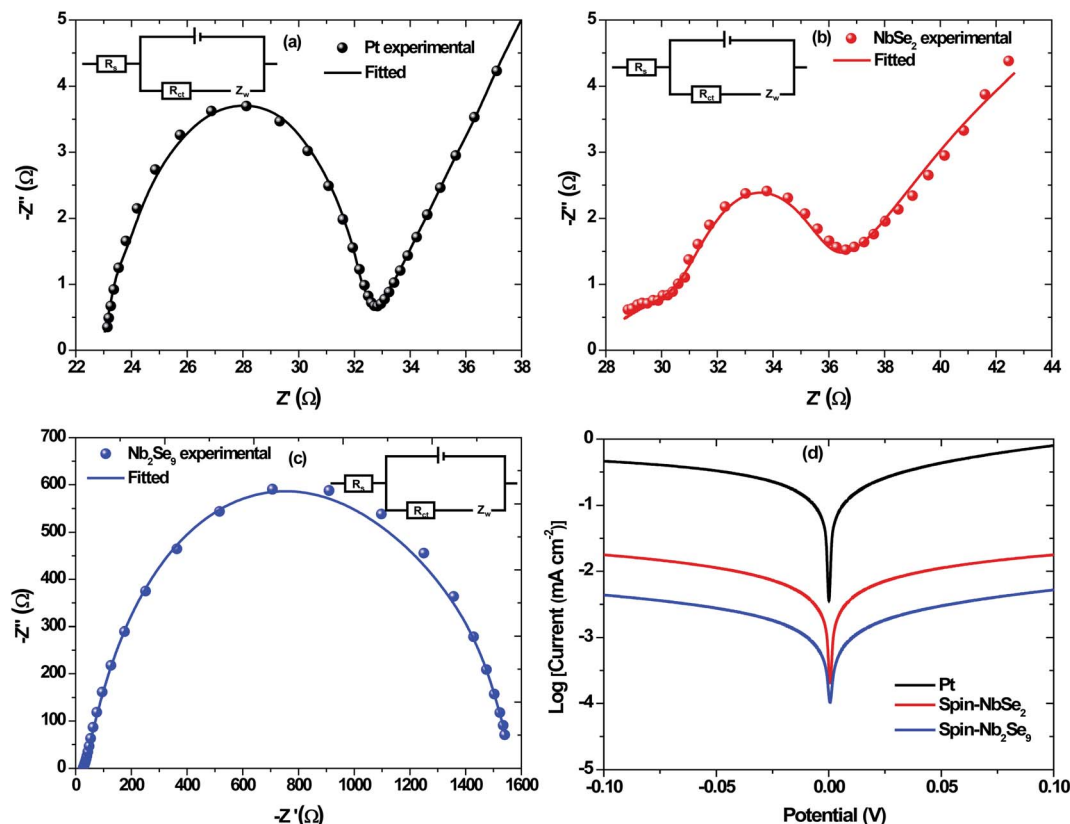$$i_{\text{p}} = 2.69 \times 10^5 n^{3/2} A D^{1/2} V^{1/2} C \qquad (8)$$

Fig. 14   Nyquist plots of EIS for the symmetric cells with (a) Pt, (b) spin–NbSe$_2$ and (c) spin–Nb$_2$Se$_9$ and the corresponding Tafel plots (d).

where i_p is the peak current density, n is the number of electrons transferred, A is the area of the electrode, D is the diffusion coefficient, V is the scan rate, and C is the concentration.[43] The scan rates were 10, 20, 50 and 100 mV s^{-1} and the results are shown in Fig. 13. Typically, there are two pairs of redox peaks where the left pair is due to the reduction of I$_3^-$ and the right pair is due to the oxidation of I$^-$ and they correspond to the following equations:

$$I_3^- + 2e^- \leftrightarrow 3I^- \tag{9}$$

$$3I_2 + 2e^- \leftrightarrow 3I_3^- \tag{10}$$

The Pt-CE, shown in Fig. 13a, is stable and reproducible irrespective of the scan rate used because the scans remained unchanged for each scan rate. The cathodic peaks appear at 0.36 V and 0.50 V. The performance of the DSSC depends on the reduction whereas as the oxidation does not have that much effect.[44] Ibrahem et al. reported that in general, the higher the cathodic current peak the better the catalytic capability of the CE towards the reduction of I$_3^-$ to I$^-$ in DSSCs.[21]

Two methods were used to fabricate the niobium selenide CEs i.e. drop casting and spin coating. The cyclic voltammograms of NbSe$_2$ nanoflowers at different scan rates (10 mV s^{-1}, 20 mV s^{-1}, 50 mV s^{-1}, and 100 mV s^{-1}) are shown in Fig. 13b and c. The current densities increase with an increase in scan

rate. The drop-casted CE has a lower current density compared to the spin-coated CE, with the value of 0.0087 A cm^{-2} and 0.0090 A cm^{-2} at a scan rate of 100 mV s^{-1}. Moreover, the drop-casted CE's cathodic peaks are not as defined as those of the spin-coated CE. Therefore, the spin-coated CE has the better catalytic capability for the reduction of I$_3^-$ to I$^-$. The Nb$_2$Se$_9$ CEs were also analyzed, and the spin-coated CE seems to have a better capability of reducing I$_3^-$ to I$^-$ than the drop-casted CE shown in Fig. 13d and e. Therefore, the Nb$_2$Se$_9$ spin-coated CE produces the desired results at 50 mV s^{-1} because it has the highest current density.

As proof of principle and to highlight the possibility of using niobium selenide CEs as alternatives to the Pt-CE, the two CEs (spin-coated: NbSe$_2$ and Nb$_2$Se$_9$) were compared with the Pt-CE. The peak-to-peak separation (E_{pp}) is an important parameter to look at when comparing the catalytic activity of electrodes.[45] The cathodic peak represents the reduction velocity and the E_{pp} is associated with the reversibility of the redox reaction.[45] The Pt-

Table 5   Electrochemical performance parameters obtained from EIS & Tafel polarization plots of Pt, spin–NbSe$_2$ and spin–Nb$_2$Se$_9$

Materials	R_s/Ω	R_{ct}/Ω	log J_0/(mA cm^{-2})	log J_{lim}/(mA cm^{-2})
Pt	23.04	9.41	−5.47	−5.38
Spin–NbSe$_2$	27.38	36.14	−6.01	−9.92
Spin–Nb$_2$Se$_9$	27.58	1033	−6.85	−12.1

CE has an E_{pp} of 805 mV whereas NbSe$_2$ and Nb$_2$Se$_9$ CEs are 819 and 762 mV, respectively. Therefore, the Nb$_2$Se$_9$-CE has better reversibility and electrocatalytic activity because it has a smaller E_{pp} than the Pt-CE. However, the NbSe$_2$-CE has a similar E_{pp} as the Pt-CE. Moreover, the NbSe$_2$-CE exhibited the highest current density compared to Nb$_2$Se$_9$-CE, which is an indication of better electrocatalytic activity. As such, of the two niobium selenide materials NbSe$_2$ is a better CE than Nb$_2$Se$_9$ because of its comparable E_{pp} and higher current density than that of Pt. This is because the NbSe$_2$ nanoflowers that are essentially nanosheets that are 'crumbled up' have the largest surface area and better coverage of the FTO-glass substrate than the Nb$_2$Se$_9$ nanorods.[45] To verify the surface area, the relationship between the current density and square root of the scan rate was plotted in Fig. 13f based on eqn (8). The electrochemical double-layer capacitance (C_{dl}) of NbSe$_2$-CE was much larger than Nb$_2$Se$_9$-CE (slope), therefore suggesting a greater effective surface area (S) ($C_{dl} \propto S$).

The EIS was employed to evaluate the ability of the CEs to transfer charge to the electrolyte. Shown in Fig. 14 are the Nyquist plots of Pt, NbSe$_2$ and Nb$_2$Se$_9$ as well as the electrochemical equivalent circuit whose components represent four impedance properties. The series resistance is denoted by, R_s while R_{ct} denotes the charge transfer resistance at the CE/electrolyte interface. The abbreviation C_{dl} corresponds to the double layer capacitance, which is employed when a perfect semi-circle is obtained from the Nyquist plot and explains the charge storage capacity of the CEs. Lastly, Z_w represents the Nernst diffusion element, often employed when a line is at 45° to the semi-circle at lower frequency region and explains if the

interaction between the CE and the electrolyte is diffusion-controlled.[46] The two key parameters, R_s and R_{ct} were obtained using Z-fit in EC-Chem software from Biologic and are summarized in Table 5. The Pt had the lowest R_s value followed by NbSe$_2$ and then Nb$_2$Se$_9$. The smaller the R_s value, the more conductive the material is. This suggests that Pt is the most conductive. The same trend was observed for R_{ct} however, the charge transfer resistance for Pt was far much lower than NbSe$_2$. Lower R_{ct} values are sort-after because they lead to higher J_{sc} and FF values. It must be added that thin-film quality has a significant influence on the electrical properties of materials. The sputtered Pt electrode had far better coverage than NbSe$_2$ and Nb$_2$Se$_9$.

The Tafel polarization curves are shown in Fig. 14d. Two important parameters are observed from the polarization curves, namely the exchange current density (J_0) and the limiting diffusion current density (J_{lim}). Both parameters are affected by the anodic or cathodic contribution of each counter electrode and can be described using the following equation;

$$J_0 = RT/nFR_{ct} \tag{11}$$

$$J_{lim} = 2nFDC/l \tag{12}$$

where R is the gas constant, T is the temperature (298 K), F is Faraday's constant, n ($n = 2$) is the number of electrons, R_{ct} is the charge transfer resistance, D the diffusion coefficient, C is the concentration of I$_3^-$, and l is the spacer thickness.[47] From eqn (11), J_0 is inversely proportional to R_{ct}. Therefore, J_0 can be correlated to the electrocatalytic activity of the CE, meaning
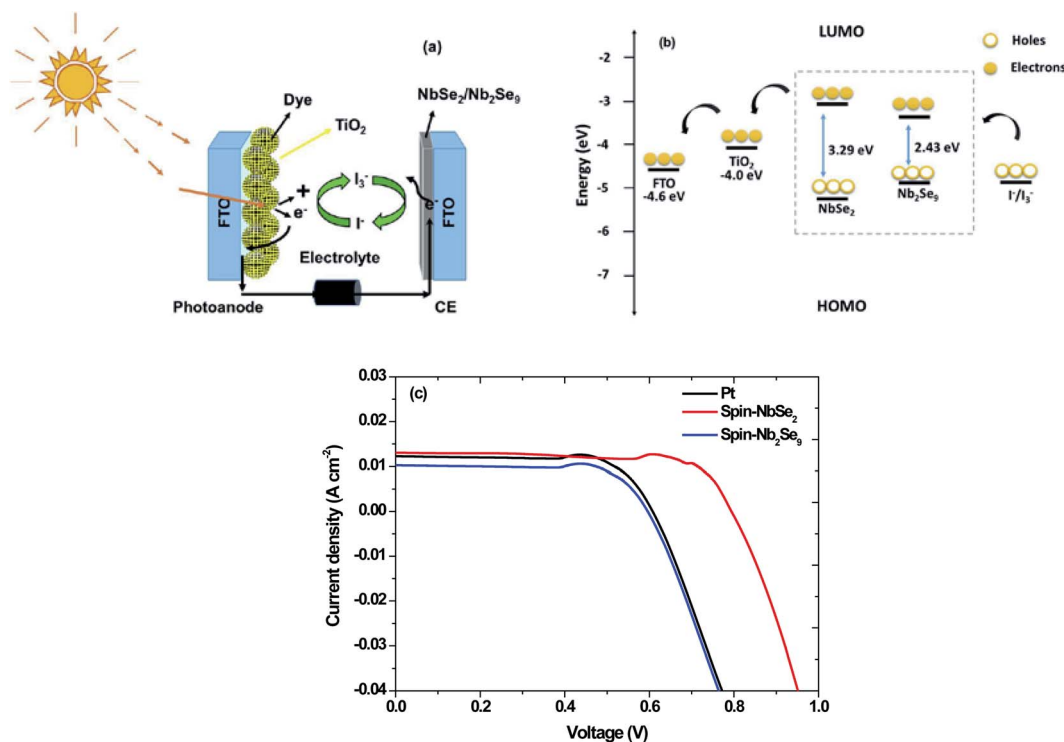

Fig. 15 (a) Dye-sensitized solar cell set-up, (b) band diagram and (c) J–V curves of DSSCs of Pt, spin-NbSe$_2$ and spin-Nb$_2$Se$_9$ counter electrodes.

Table 6 $J–V$ parameters of DSSCs of Pt, spin-NbSe$_2$ and spin-Nb$_2$Se$_9$ counter electrodes

Counter electrode	J_{sc} (mA cm^{-2})	V_{oc} (V)	FF (%)	PCE (%)
Pt	12.00	0.77	34	3.14
Spin-NbSe$_2$	13.00	0.95	55	6.84
Spin-Nb$_2$Se$_9$	10.00	0.76	37	2.80

a large J_0 value implies a much better catalytic activity. Similarly, larger J_{lim} values indicate the larger diffusion coefficient D, which results in higher catalytic activity based on eqn (12). The J_0 value of NbSe$_2$ was higher than Nb$_2$Se$_9$ symbolizing the best electrocatalytic activity. So too was the J_{lim} value. In both the EIS analysis and Tafel polarization curves, Pt was the best performing electrode. This was not surprising as Pt is considered the state-of-the-art counter electrode, furthermore visually; the Pt thin film was uniform.

The Pt, NbSe$_2$ and Nb$_2$Se$_9$ CEs were used in DSSCs. Shown in Fig. 15 is the solar cell architecture, band structure and the resultant current density–voltage ($J–V$) curves of the three CEs and the results are also summarized in Table 6. The NbSe$_2$ solar cell had the highest PCE of 6.84% compared to the other electrodes. This was in the same order as the reported results for NbSe$_2$ DSSCs.[21] The Pt base DSSC surprising had a lower efficiency, contrary to the electrochemical results. This could be because of the fabrication process. The Nb$_2$Se$_9$ had the lowest efficiency, which is consistent with the electrochemical data. The superior performance of NbSe$_2$ over Nb$_2$Se$_9$ can be attributed to the morphology of the nanostructures. The NbSe$_2$ nanoflowers has a larger apparent surface area compared to Nb$_2$Se$_9$ nanorods. Also notably from Fig. 15 and the data in Table 6 are the low FF values. The low FF values are due to the high R_s values and low shunt resistance (R_{sh}) values, which are caused by increasing recombination at interfaces of the DSSCs.[48]

4. Conclusion

In summary, niobium selenide nanostructures were formed using the colloidal method. Varying the metal precursors resulted in the formation of different stoichiometries of niobium selenide. The NbCl$_5$ and NbF$_5$ resulted in the formation of NbSe$_2$ and Nb$_2$Se$_9$, respectively. While maintaining the two different metal precursors and varying the selenium precursor from Se, SeO$_2$ to SU, the properties of NbSe$_2$ and Nb$_2$Se$_9$ changed slightly however the effect of changing the selenium precursor was less pronounced than changing the metal precursors. From the XRD and XPS, the NbSe$_2$ nanostructures were more susceptible to oxidation than Nb$_2$Se$_9$ as Nb$_2$O$_5$ was observed in the XRD and the percentage of M–O in the XPS was much higher in NbSe$_2$. The nanostructures were capped by OLA as observed in the FT-IR spectroscopy thus minimizing the oxidation. NbSe$_2$ generally formed nanoflowers whilst Nb$_2$Se$_9$ formed rods. The band-gaps of both NbSe$_2$ and Nb$_2$Se$_9$ were in the visible region and there were red-shifted as

the selenium precursor was altered. The spin coated NbSe$_2$ and Nb$_2$Se$_9$ were used successfully as electrocatalysts in DSSCs. NbSe$_2$ nanoflowers gave the best performance with 6.84% PCE.

Conflicts of interest

There are no conflicts to declare.

Acknowledgements

References

1 S. Memaran, N. R. Pradhan, Z. Lu, D. Rhodes, J. Ludwig, Q. Zhou, O. Ogunsolu, P. M. Ajayan, D. Smirnov and D. Fernández-Domínguez, *Nano Lett.*, 2015, **15**, 7532–7538.

2 S. M. M. Nelwamondo, M. J. Moloto, R. W. Krause and N. Moloto, *Mater. Res. Bull.*, 2012, **47**, 4392–4397.

3 L. F. E. Machogo, P. Tetyana, R. Sithole, S. S. Gqoba, N. Phao, M. Airo, P. M. Shumbula, M. J. Moloto and N. Moloto, *Appl. Surf. Sci.*, 2018, **456**, 973–979.

4 C. Lee, X. Wei, J. W. Kysar and J. Hone, *Science*, 2008, **321**, 385–388.

5 S. Chae, A. J. Siddiqa, S. Oh, B. J. Kim, K. H. Choi, W. Jang, Y. Kim, H. K. Yu and J. Choi, *Nanomaterials*, 2018, **8**(10), 794.

6 P. Joensen, R. F. Frindt and S. R. Morrison, *Mater. Res. Bull.*, 1986, **21**, 457–461.

7 M. A. Ibrahem, W.-C. Huang, R.-W. Lan, K. M. Boopathi, Y. C. Hsiao, C. H. Chen, C.-S. Chang, L.-J. Li, C.-H. Tsai and C. W. Chu, *J. Mater. Chem. A*, 2014, **2**, 11382–11390.

8 R. Qu, X. Wen, Y. Zhao, T. Wang, R. Yao and J. Lu, *Ultrason. Sonochem.*, 2021, **73**, 105491.

9 J. Liu, X. Sui, S. Zhang, S. Xu and J. Hao, *Tribology*, 2018, **38**, 635–644.

10 T. Tsuneta, T. Toshima, K. Inagaki, T. Shibayama, S. Tanda, S. Uji, M. Ahlskog, P. Hakonen and M. Paalanen, *Curr. Appl. Phys.*, 2003, **6**, 473–476.

11 F. O.-T. Agyapong-Fordjour, S. Oh, J. Lee, S. Chae, K. H. Choi, S. H. Choi, S. Boandoh, W. Yang, J. Huh, K. K. Kim and J.-Y. Choi, *ACS Appl. Energy Mater.*, 2019, **2**, 5785–5792.

12 B. J. Kim, B. J. Jeong, S. Oh, S. Chae, K. H. Choi, T. Nasir, S. H. Lee, K.-W. Kim, H. K. Lim, I. J. Choi, L. Chi, S.-H. Hyun, H. K. Yu, J.-H. Lee and J.-Y. Choi, *RSC Adv.*, 2018, **8**, 37724–37728.

13 F. Kadijk and F. Jellinek, *J. Less-Common Met.*, 1971, **23**, 437–441.

14 P. Sekar, E. C. Greyson, J. E. Barton and T. W. Odom, *J. Am. Chem. Soc.*, 2005, **127**, 2054–2055.

15 J. Guo, Y. Shi, C. Zhu, L. Wang, N. Wang and T. Ma, *J. Mater. Chem. A*, 2013, **1**, 11874–11879.

16 V. K. Lamer and R. H. Dinegar, *J. Am. Chem. Soc.*, 1950, **72**(11), 4847–4854.

17 J. Van Embden, A. S. R. Chesman and J. J. Jasieniak, *Chem. Mater.*, 2015, **27**, 2246–2285.

18 M. Wu, Y. Wang, X. Lin, N. Yu, L. Wang, L. Wang, A. Hagfeldt and T. Ma, *Phys. Chem. Chem. Phys.*, 2011, **13**, 19298–19301.

19 E. Singh, K. S. Kim, G. Y. Yeom and H. S. Nalwa, *RSC Adv.*, 2017, 7, 28234.

20 J. Liang, J. Li, H. Zhu, Y. Han, Y. Wang, C. Wang, Z. Jin, G. Zhang and J. Liu, *Nanoscale*, 2016, **8**, 16017–16025.

21 M. A. Ibrahem, W. Huang, T. Lan, K. M. Boopathi, Y. Hsiao, C. Chen, W. Budiawan, Y. Chen, C. Chang, L. Li, C. Tsai and C. W. Chu, *J. Mater. Chem. A*, 2014, **2**, 11382.

22 J. Guo, Y. Shi, C. Zhu, L. Wang, N. Wang and T. Ma, *J. Mater. Chem. A*, 2013, **1**, 11874–11879.

23 S. B. Artemkina, T. Y. Podlipskaya, A. I. Bulavchenko, A. I. Komonov, Y. V. Mironov and V. E. Fedorov, *Colloids Surf., A*, 2014, **461**, 30–39.

24 W. Lee, S. Chae, Y. K. Chung, S. Oh, J. Choi and J. Huh, *Phys. Status Solidi RRL*, 2018, 1800517.

25 R. Sanjines, H. Berger and F. Levy, *Mater. Res. Bull.*, 1988, **23**, 549–553.

26 S. Naik, G. K. Pradhan, S. G. Bhat, B. C. Behera, P. S. A. Kumar, S. L. Samal and D. Samal, *Phys. C*, 2019, **561**, 18–23.

27 J. Lee, B. J. Kim, Y. K. Chung, W. Lee, I. J. Choi, S. Chae, S. Oh, J. M. Kim, J. Choi and J. Huh, *J. Raman Spectrosc.*, 2020, **51**, 1100–1107.

28 M. Devaraj, R. Saravanan, R. Deivasigamani, V. K. Gupta, F. Gracia and S. Jayadevan, *J. Mol. Liq.*, 2016, **221**, 930–941.

29 R. K Sithole, L. F. E. Machogo, M. A. Airo, S. S. Gqoba, M. J. Moloto, P. Shumbula, J. Van Wyk and N. Moloto, *New J. Chem.*, 2018, **42**, 3042–3049.

30 N. D. Boscher, C. J. Carmalt and I. P. Parkin, *Eur. J. Inorg. Chem.*, 2006, 1255–1259.

31 S. Cao, T. Liu, W. Zeng, S. Hussain, X. Peng and F. Pan, *J. Mater. Sci.: Mater. Electron.*, 2014, **25**, 4300–4305.

32 A. Prabakaran, F. Dillon, J. Melbourne, L. Jones, R. J. Nicholls, P. Holdway, J. Britton, A. A. Koos, A. Crossley, P. D. Nellist and N. Grobert, *Chem. Commun.*, 2014, **50**, 12360–12362.

33 S. H. Ahn and A. Manthiram, *Adv. Energy Mater.*, 2016, **6**, 1–7.

34 R. G. Pearson, *J. Chem. Educ.*, 1968, **45**, 643–648.

35 J. Chatt, *Nature*, 1956, **177**, 852.

36 F. A. Cotton and G. Wilkinson, *Advanced Inorganic Chemistry*, John Wiley & Sons, New York, 5th edn, 1988.

37 W. Hönle, S. Furuseth and H. G. Schnering, *Z. Naturforsch., B: J. Chem. Sci.*, 1990, **45**, 952–956.

38 A. F. Holleman, E. Wiberg and N. Wiberg, *Inorganic Chemistry*, 2001.

39 N. Savjani, E. A. Lewis, M. A. Bissett, J. R. Brent, R. A. Dryfe, S. J. Haigh and P. O'Brien, *Chem. Mater.*, 2016, **28**(2), 657–664.

40 F. A. Devillanova, *Handbook of Chalcogen Chemistry: New Perspectives in Sulfur, Selenium and Tellurium*, Royal Society of Chemistry, 2007, ISBN 9780854043668.

41 B. Xu, X. Ma, J. Tian, F. Zhao, Y. Liu, B. Wang, H. Yang and Y. Xia, *Ionics*, 2019, **25**, 4171–4177.

42 Q. Shi, H. Zhu and L. Dang, *J. Phys.: Conf. Ser.*, 2020, **1549**, 032085.

43 M. Wu, Y. Wang, X. Lin, N. Yu, L. Wang, L. Wang, A. Hagfeldt and T. Ma, *Phys. Chem. Chem. Phys.*, 2011, **13**, 19298–19301.

44 Z. Huang, X. Liu, K. Li, D. Li, Y. Luo, H. Li, W. Song, L. Chen and Q. Meng, *Electrochem. Commun.*, 2007, **9**, 596.

45 J. Roy-Mayhew, D. Bozym, C. Punckt and I. Aksay, *ACS Nano*, 2010, **4**, 6203.

46 G. Yue, W. Wu, X. Liu and H. Zheng, *Sol. Energy*, 2018, **167**, 137–146.

47 X. Qian, H. Li, L. Shao, X. Jiang and L. Hou, *ACS Appl. Mater. Interfaces*, 2016, **8**, 29486–29495.

48 Z. Huang, G. Natu, Z. Ji, M. He, M. Yu and Y. Wu, *J. Phys. Chem. C*, 2012, **116**, 26239–26246.